Journal of Photopolymer Science and Technology
Volume 33, Number 5 (2020) 583 – 590 ©2020SPST

Analysis of Pressure-induced Variations in the Crystalline Structures of Polyimides Having Flexible Linkages by Wide-Angle X-ray Diffraction

Koichiro Muto, Eisuke Fujiwara, Ryohei Ishige, and Shinji Ando*

Department of Chemical Science and Engineering, Tokyo Institute of Technology, 2-12-1-E4-5-308, Ookayama, Meguro-ku, Tokyo 152-8552, Japan
**sando@polymer.titech.ac.jp*

Pressure-induced variations in the crystalline structures of polyimides (PIs) that have flexible ether or thioether linkages along the main chain were analyzed by synchrotron wide-angle X-ray diffraction at high pressures up to 2.0 GPa. The crystalline lattices of poly(4,4-oxidiphenylene pyromellitimide) (PMDA/ODA) and poly(4,4'-diamino-diphenyl sulfide pyromellitimide) (PMDA/SDA) PIs that have one flexible linkage in their repeating unit showed negative linear compressibility along the main-chain direction (*c*-axis), with a large anisotropy in the compressibilities between the two interchain directions (*a*- and *b*-axes). In contrast, polyimides prepared from bis(4-aminophenyl) ether (PMDA/TPE) and 4,4'-bis(4-aminophenoxy) biphenyl (PMDA/BAPB) that have two flexible linkages in their repeating units exhibited positive compressibility along the main-chain direction, with a small difference in compressibility between the interchain directions. The different compression behaviors of PI crystalline lattices can be explained by the intrinsic Λ-shaped conformation of PMDA/ODA and PMDA/SDA, specifically the rotational fluctuations of the phenyl groups of the diamine moiety that were induced by the applied pressure.

Keywords: Polyimide, Crystal structure, Synchrotron wide-angle X-ray diffraction, High pressure, Negative compressibility

1. Introduction

Fully aromatic polyimides (PIs) are well-known super engineering plastics that exhibit outstanding thermal and chemical stability, flame resistance, radiation resistance, mechanical strength, and flexibility [1]. Owing to their very high performance, PIs have been widely used in the aerospace, electric, electronic, and optical industries [2]. The molecular aggregation structures of PI chains in films have been intensively investigated because the thermal, mechanical, electrical, and optical properties of PI films are significantly influenced by the higher order structures of PI chains. For example, Hasegawa *et al*. [3] reported that the fluorescence intensity of the poly(*trans*-1,4-cyclohexyl-biphenyltetracarboximide) (*s*-BPDA/CHDA PI) decreased with an increase in the imidization temperature (T_i), suggesting that denser aggregation can enhance intermolecular interactions such as π–π stacking and possibly affect the optical properties of PIs.

The molecular aggregation structures of PIs have been mainly investigated by wide-angle X-ray diffraction (WAXD) [4–19]. Russell *et al*. [13] reported that poly(4,4-oxidiphenylene pyromellitimide) (PMDA/ODA) films exhibited different aggregation structures ranging from amorphous to highly ordered crystalline depending on the film thickness and preparation conditions. However, PI films do not necessarily exhibit definitive crystalline diffraction peaks due to their low crystallinity. Hence, several research groups have focused on PI powders or oriented fibers that have high crystallinity to examine crystalline or ordered structures. Okuyama *et al*. [9,14] investigated highly crystalline fibers of poly(4,4-diphenylene pyromellitimide) (PMDA/BZ) prepared through a process that included wet-spinning from *N*-methyl-2-pyrrolidone (NMP) solutions of poly(amic acid) (PAA) and subsequent thermal and chemical

Received March 18, 2020
Accepted April 14, 2020

imidization. Kimura *et al*. [16,17] synthesized aromatic PI powders using phase separation techniques during solution imidization, and the prepared powders exhibited high crystallinity and various morphologies. Recently, we evaluated the coefficients of linear and volumetric thermal expansion (CTE and CVE, respectively) of the crystal lattices of thirteen kinds of PIs by variable temperature WAXD measurements [5]. The CTE and anisotropy of these PIs strongly depended on their molecular structures, whereas the CVE of these PIs were closely related to the weight density of the crystallites regardless of their chemical structure.

Applying a high pressure to induce external perturbation onto the aggregation structures of polymer chains in the solid state is more effective than varying temperature. We have measured WAXD patterns [18–22], infrared absorption (IR) [23,24], ultraviolet/visible (UV/Vis) absorption, fluorescence spectra [25–33], and Brillouin scattering spectra [34] of various PIs under high pressure in order to examine the relationships between the molecular aggregation structures and the physical and optical properties in the solid state. Recently, we discovered that the optical properties of PI films are well correlated with their molecular aggregation structures based on the UV/Vis absorption and fluorescence spectra at elevated pressures up to 8.0 GPa [33]. A gradual bathochromic shift of the absorption bands and a significant reduction in the fluorescence intensity are mainly attributable to the compression of the interchain free volume below 2.0 GPa and to the deformation of the molecular chain above 2.0 GPa. On the other hand, we have reported pressure-induced variations in the crystalline and ordered structures of PIs using synchrotron WAXD measurements at high pressures [18,19]. The crystalline lattices of rigid-rod PIs showed typical compression behaviors; specifically, each crystal axis was monotonically compressed after increasing the pressure. In contrast, the crystalline lattice of PMDA/ODA having only one flexible ether linkage in the main chain showed a characteristic negative compressibility along the main-chain direction (*c*-axis) at high pressures up to 1.0 GPa. The mechanism of this anomalous lattice expansion in PIs has not been clarified yet.

In this study, semi-crystalline powders of aromatic PIs derived from pyromellitic acid dianhydride (PMDA) and four kinds of diamines with flexible ether linkages (Chart 1) were synthesized, and the compression behaviors of the crystalline lattice of these PIs were precisely measured and analyzed by synchrotron WAXD measurements at elevated pressures up to 2.0 GPa.

2. Experimental

2.1. Materials

PMDA was purchased from Tokyo Kasei Kogyo Co. Ltd. (Tokyo, Japan) and purified by drying at 120 °C for 3 h in vacuo followed by sublimation under reduced pressure. 4,4′-Diaminodiphenyl ether (ODA), 4,4′-diamino-diphenyl sulfide (SDA), and hydroquinone bis(4-aminophenyl) ether (TPE) purchased from Tokyo Kasei Kogyo Co. Ltd (Tokyo, Japan) and 4,4′-bis(4-aminophenoxy) biphenyl (BAPB) purchased from Wako Pure Chemical Industries Ltd. (Osaka, Japan) were purified by sublimation under reduced pressure. Anhydrous *N*-methyl-2-pyrrolidone (NMP) was purchased from Sigma-Aldrich Japan (Tokyo, Japan) and used without further purification.

2.2. Sample preparation

The chemical structures of the four PIs prepared from the monomers mentioned above, PMDA/ODA, PMDA/SDA, PMDA/TPE, and PMDA/BAPB, are shown in Chart 1. The highly crystalline PI powders were prepared by the *in situ* thermal imidization technique [6]. First, each diamine was dissolved in NMP, and then an equimolar amount of PMDA was added and the solution was stirred at 22 °C for 48 h to form a solution of poly(amic acid) (PAA), the precursor of these PIs. Second, the PAA solution was refluxed at 200−210 °C for 4 h under a N_2 atmosphere with stirring, and then a crystalline PI powder was precipitated from the solution after cooling to 22 °C. Crude PI powder was washed with NMP and distilled water several times, followed by drying at 100 °C in vacuo for 1 h. Finally, a highly crystalline PI powder was obtained by annealing the samples at 200 °C and then at 400 °C under a N_2 atmosphere for 1 h to remove residual NMP, complete thermal imidization, and promote subsequent crystallization.

2.3. Measurements

Experimental procedures using a high-pressure diamond anvil cell (DAC) have been described elsewhere [20]. The ruby fluorescence technique was used to estimate the pressure inside the sample chamber [35], and a mixture of three kinds of silicone oils (KF-96-500CS, KF-50-300CS, and KF-50-1000CS, Shin-Etsu Co., Ltd., Japan) in a

weight ratio of 2:1:1 was used as the pressure medium. Owing to the limited volume of the sample chamber (300 μm in diameter), transmission X-ray diffraction measurements were performed with a BL-10C beamline at the Photon Factory (KEK, Tsukuba, Japan) using a PILATUS3 2M detector (Dectris, Baden-Daetwill, Switzerland). The wavelength of the X-ray was set to 0.089 nm. Broad scattering from the silicone oil was subtracted from the diffraction patterns measured at each pressure. The camera length was calibrated using the 00*l* diffractions from lead stearate as the standard.

2.4. Density functional theory calculations

Density functional theory (DFT) was used to calculate the optimized geometry of one repeating unit of the aromatic PIs. The B3LYP(Becke, 3-parameter, Lee-Yang-Parr) hybrid functional was selected for these computations, and the 6-311G(d) basis set was used for geometry optimization. All calculations were performed using the Gaussian 16 Rev.A03 software package, available via the Global Scientific Information and Computing Center (GSIC), Tokyo Institute of Technology.

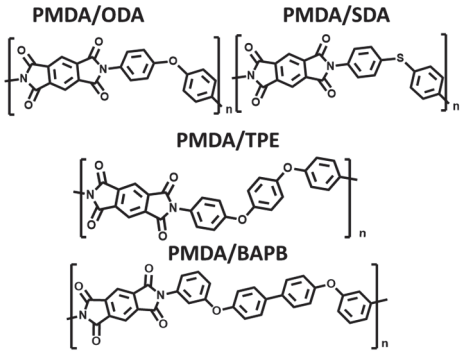

Chart 1. Chemical structures of the polyimides.

3. Results and discussion

3.1. Crystal structures of PIs

Figure 1 shows the transmission X-ray diffraction patterns of PI powders measured at atmospheric pressure (0.1 MPa). The crystalline cell structures of these PIs were assigned as orthorhombic ($\alpha = \beta = \gamma = 90°$) except for the monoclinic symmetry ($\alpha = 98.4°$) of PMDA/TPE. The diffraction peaks were indexed on the basis of previous reports on fiber X-ray diffraction [5,7–9]. The lattice parameters of the *a*-, *b*-, and *c*-axes were quantitatively estimated because these PIs exhibit (00*l*) peaks corresponding to periodic structures along the main chains, as well as several (*hk*0) peaks corresponding to intermolecular ordering structures. Table 1 shows the lattice parameters of the PIs at atmospheric pressure. The crystal density ρ was calculated based on the molecular weight of a repeating unit of the selected PI, the lattice volume calculated from lattice parameters (*a*, *b*, *c*), and the number of repeating units in a unit cell.

Table 1. Lattice parameters and weight density of the polyimide crystals.

polyimide sample	lattice parameter				
	a(Å)	*b*(Å)	*c*(Å)	*Z*	ρ (g/cm^3)
PMDA/ODA	6.27	3.79	31.44	2	1.70
PMDA/SDA	6.39	3.95	31.11	2	1.68
PMDA/TPE[a]	8.12	5.56	20.91	2	1.67
PMDA/BAPB	8.05	6.36	24.44	2	1.47

[a]Monoclinic lattice with $\alpha = 98.4°$. The other crystal lattices were assigned as orthorhombic ($\alpha = \beta = \gamma = 90°$).

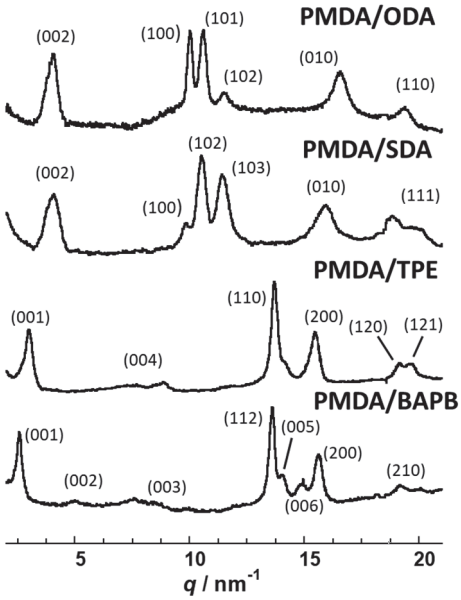

Fig. 1. Wide-angle synchrotron X-ray diffraction profiles of PMDA/ODA, PMDA/SDA, PMDA/TPE, and PMDA/BAPB PI powders at atmospheric pressure.

Here, the molecular packing structure of PMDA/SDA in the crystal lattice was assumed to be similar to one of the probable crystal structures of PMDA/ODA [5], as shown in Fig. 2, because of the similarity between their primary structures. Specifically, two sequential repeating units of PMDA/SDA were accommodated in a P1 orthorhombic lattice, in agreement with the reported diffraction patterns [7].

Comparing lattice parameters along the *c*-axis (*c*), PMDA/SDA had a slightly smaller *c* value than PMDA/ODA. Based on the model, this difference could originate from differences in the bond lengths and/or bond angles at the bent linkages of ether (−O−) and thioether (−S−) in the diamine moieties

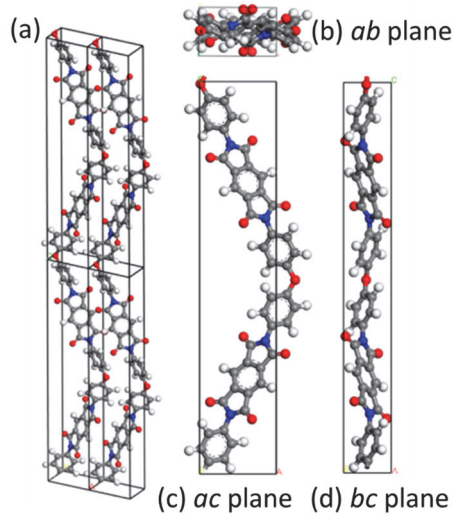

Fig. 2. (a) One of the probable crystal structures of PMDA/ODA. Projections of the lattice on (b) *ab* plane, (c) *ac* plane, and (d) *bc* plane [5].

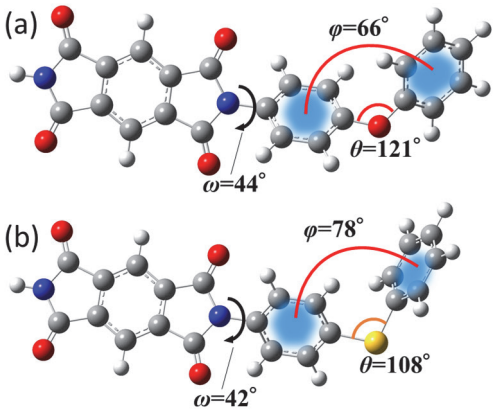

Fig. 3. Optimized geometries of the repeating units of (a) PMDA/ODA and (b) PMDA/SDA using density field theory.

because the conformation along the main chain does not cause significant differences in the value of *c*. The C–S bond length in diphenylthioether (1.762 Å) [36] was reported to be 26.4% longer than the C–O bond length in diphenylthioether (1.394 Å) [37], although the C–S–C bond angle ($\theta_{C\text{–}S\text{–}C}$) of the former (106.2°) is significantly smaller than the C–O–C bond angle ($\theta_{C\text{–}O\text{–}C}$) of the latter (118.3°). Prokopchuk *et al*. [38] presumed the $\theta_{C\text{–}S\text{–}C}$ of PMDA/SDA is 110°, a significantly smaller value than the reported $\theta_{C\text{–}O\text{–}C}$ of PMDA/ODA (121°−126°) [8,10]. Furthermore, the $\theta_{C\text{–}O\text{–}C}$ and $\theta_{C\text{–}S\text{–}C}$ angles are 121° and 108°, respectively, in the geometries optimized by the DFT calculations for PMDA/ODA and PMDA/SDA (See Fig. 3). Thus, the smaller *c* value of the PMDA/SDA lattice than that of PMDA/ODA is mainly attributable to the difference in the bond angles at the diamine moieties where $\theta_{C\text{–}S\text{–}C}$ is smaller than $\theta_{C\text{–}O\text{–}C}$.

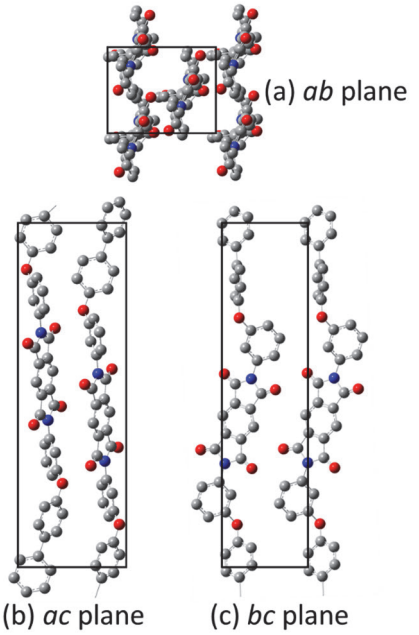

Fig. 4. Crystal structure of PMDA/BAPB. Projections on the (a) *ab* plane, (b) *ac* plane, and (c) *bc* plane [9].

On the other hand, the crystal structures of PMDA/TPE and PMDA/BAPB are distinctly different from those of PMDA/ODA and PMDA/SDA [8,9], as shown in Fig. 4. Two molecular chains extend through the crystal lattice and the projected length of one repeating unit corresponds to the *c* value of PMDA/TPE and PMDA/BAPB, whereas the projected length of two repeating units corresponds to the *c* value of PMDA/ODA and PMDA/SDA.

3.2. Compression behaviors of PI powders

Figure 5 shows the pressure-induced variations in the diffraction patterns of the PI powders. The lattice parameters along the *a*-, *b*-, and *c*-axes (*a*, *b*, and *c*) were measured at each pressure and used to calculate the strain (ε) quantitatively. A strain (*i.e.* deformation) at *P* GPa is defined as $\Delta d/d_0$, where d_0 is the lattice parameter at atmospheric pressure (0.1 MPa) and Δd is the variation in the lattice parameter with increasing pressure from 0.1 MPa to *P* GPa. Figures 6 and 7 show the variations in ε values along the *a*-, *b*-, and *c*-axes (ε_a, ε_b, and ε_c) for all the PIs. The values of *a*, *b*, and *c* for PMDA/TPE at higher pressures were determined by fixing the interaxis angles of the crystalline lattice to the following values, $\alpha = 98.4°$, $\beta = 90°$, and $\gamma = 90°$. Table 2 lists the ε_a, ε_b, and ε_c values estimated at 2.0 GPa for each PI. The positive local maximum values of ε_c for PMDA/ODA and PMDA/SDA were observed at 1.5 GPa and 2.5 GPa, respectively.

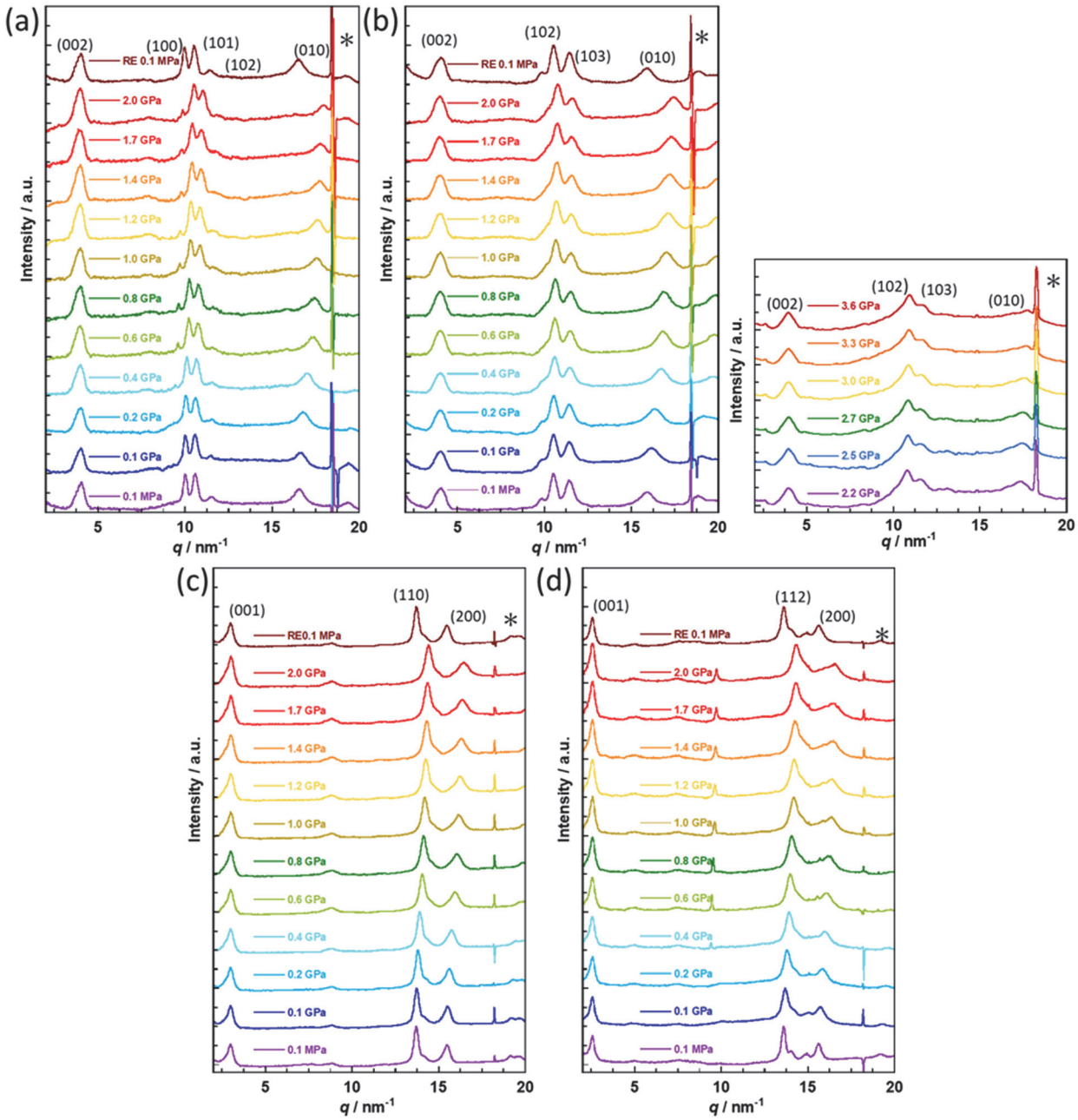

Fig. 5. Pressure-induced variations in the diffraction patterns of the PI powders, (a) PMDA/ODA, (b) PMDA/SDA, (c) PMDA/TPE, (d) PMDA/BAPB. The peak indicated with an asterisk is the diffraction of a ruby particle used as pressure indicator.

Table 2. Strain along each crystalline axis at ca. 2.0 GPa and thermal expansion between 110 °C and 300 °C for each PI [5].

Polyimide	ε at 2.0 GPa (%)				Thermal expansion from 110 to 300 °C (%)		
	ε_a	ε_b	ε_c	ε_c^{max}	C_a	C_b	C_c
PMDA/ODA	−4.0	−7.8	+0.8	+1.2	−0.8	+3.5	−0.1
PMDA/SDA	−2.8	−8.8	+1.1	+1.5	–	–	–
PMDA/TPE	−5.9	−4.6	−0.95	–	–	–	–
PMDA/BAPB	−6.3	−5.2	−0.37	–	+2.2	+1.5	+0.1

*ε_c^{max} denotes the maximum values of strain observed for PMDA/ODA and PMDA/SDA at 1.5 and 2.5 GPa, respectively.

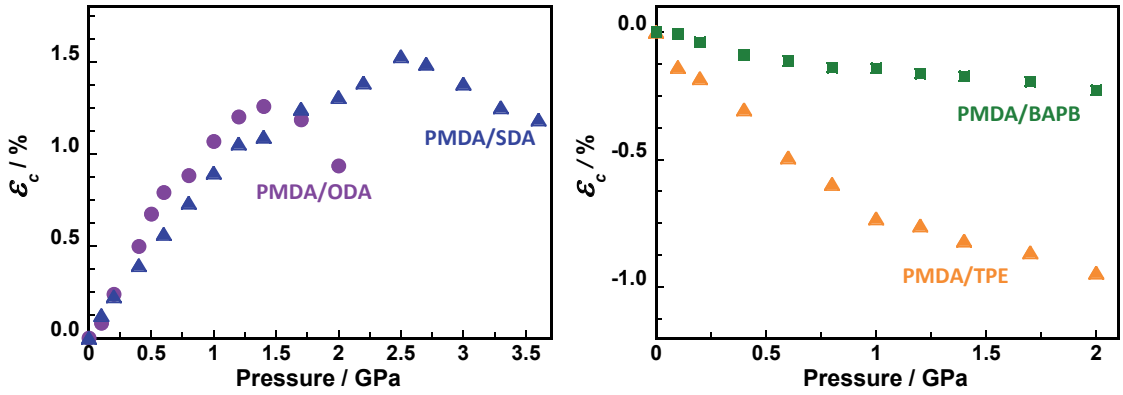

Fig. 6. Variations in the ε values along the c-axis of (a) PMDA/ODA and PMDA/SDA, (b) PMDA/TPE and PMDA/BAPB with increasing pressure up to 3.5 and 2.0 GPa, respectively.

As illustrated in Fig. 6(a) and Table 2, PMDA/ODA and PMDA/SDA showed extraordinary negative compressibility (expansion) along the c-axis up to 1.5 and 2.5 GPa, respectively. Takizawa *et al*. [19] reported that the increase in the periodic length of the PMDA/ODA chain at elevated pressures is mainly caused by an increase in θ_{C-O-C}. Similarly, the ε_c value of PMDA/SDA increased because of an increase in θ_{C-S-C} that was induced by concentrated compressive stress at the thioether linkage. When the pressures of PMDA/ODA and PMDA/SDA were above 1.5 and 2.5 GPa, respectively, these polymers exhibited decreases in c that are attributable to narrowing of the bond angles, θ_{C-O-C} and θ_{C-S-C}. Moreover, PMDA/SDA showed a larger local maximum of ε_c than that of PMDA/ODA. We have reported that the thermal expansion from 110 °C to 300 °C of the crystal lattice of PMDA/ODA, leads to an increase of lattice parameter b by 3.5%, whereas parameters a and c decrease by 0.8% and 0.1%, respectively [5]. The negative thermal expansions along the a- and c-axes can be correlated to rotational fluctuations around the p-phenylene rings of the ODA moiety at higher temperatures. One of the characteristic features of PMDA/ODA is its planar lattice conformation where the p-phenylene rings of the ODA moiety are nearly parallel to the ac plane (see Fig. 2) [5]. In this model, activated rotational fluctuations around the p-phenylene rings at high temperatures reduce intramolecular steric hindrance in the ac plane, possibly inducing decreases in parameters a and c with increasing temperature. Lattice compression is the reverse phenomenon of lattice thermal expansion [24], so parameter c could increase with increasing bond angles, specifically θ_{C-O-C} and θ_{C-S-C}, at high pressure to release intramolecular steric hindrance in the ac plane induced by the decrease in the torsional angle of the p-phenylene rings in the diamine moieties. Thus, the values of ε_c for PMDA/SDA and PMDA/ODA are closely related to widening the bent angles at high pressures.

The torsional angles between two p-phenylene rings in the ODA and SDA moieties were estimated to be 66° and 78°, respectively, based on the optimized geometries of PMDA/ODA and PMDA/SDA (See Fig. 3). In addition, the calculated spring constants for the scissoring vibrations of C−O−C in diphenyl ether and C−S−C in diphenyl thioether using the DFT method are 108 $N \cdot m^{-1}$ and 66 $N \cdot m^{-1}$, respectively. These results indicate that the angle θ_{C-S-C} is more easily deformed than θ_{C-O-C}. These results also support that the degree of pressure-induced variations in the torsional angle could be larger for PMDA/SDA than PMDA/ODA.

On the other hand, PMDA/TPE and PMDA/BAPB showed no negative compressibility along the c-axis despite their plural ether (−O−) linkages, as seen in Fig. 6(b). This observation may indicate that the TPE and BAPB moieties do not cause significant conformational changes with increasing pressure as observed for the ODA and SDA moieties.

As shown in Fig. 7(a), PMDA/ODA and PMDA/SDA exhibited large anisotropy between ε_a and ε_b; that is, the lattice is more compressible along the b-axis than the a-axis with increasing pressure. Since the b-axis corresponds to the cofacial stacking direction of phenyl and imide rings in both PIs (See Fig. 2), the significant compression along the b-axis indicates that the cofacial stacking direction is more compressible. In contrast, the relatively small compressibility along the a-axis can be correlated to the conformational freedom between the two p-phenylene rings of the ODA or SDA moiety. Namely, an increase in a caused by conformational changes at elevated pressures could release internal stress and suppress the compression

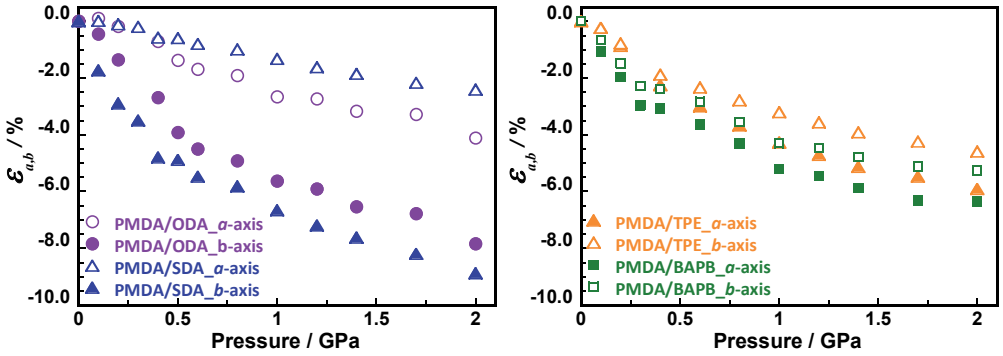

Fig. 7. Variations in ε values along the *a*- and *b*-axes of (a) PMDA/ODA and PMDA/SDA, (b) PMDA/TPE and PMDA/BAPB with increasing pressure up to 2.0 GPa.

along the *a*-axis. Another remarkable point is that PMDA/SDA had a larger anisotropy between ε_a and ε_b than PMDA/ODA. As mentioned above, the degree of pressure-induced variations in the torsional angle between two *p*-phenylene rings could be larger for PMDA/SDA than that of PMDA/ODA. Hence, the fact that the *a*-axis of PMDA/SDA is less compressible than that of PMDA/ODA could be explained by significant pressure-induced conformational change of the former.

On the other hand, PMDA/TPE and PMDA/BAPB exhibited relatively small anisotropy in linear compressibility along the *a*- and *b*-axes in Fig. 7(b). The larger compression along both the *a*- and *b*-axes of PMDA/BAPB than that of PMDA/TPE could be caused by the relatively lower weight density of the crystalline lattice in the former (See Table 1). Okuyama *et al.* [9] determined the molecular packing structure of the crystalline lattice of PMDA/BAPB and reported that the phenyl rings of the BAPB moiety do not adopt planar conformations and are parallel to neither the *ac* plane nor the *bc* plane (See Fig. 4). In addition, we have reported that PMDA/BAPB exhibits relatively small anisotropy in the linear thermal expansion between the *a*- and *b*-axes due to the twisted conformation of the lattice [5]. This previous study shows a good correlation with the isotropic compression behavior of the *ab* plane and also explains the decrease in *c* of PMDA/BAPB at elevated pressure. In other words, the isotropic compression of PMDA/BAPB induces neither significant change of the torsional angle around the ether linkage nor increases the bond angle θ_{C-O-C}. This consideration is applicable to other aromatic polymers that have bent, flexible linkages and will benefit the design of polymers with low linear compressibility and thermal expansion.

4. Conclusion

The WAXD patterns observed for powder samples of four kinds of fully aromatic PIs that have flexible ether or thioether linkages were determined at elevated pressures up to 2.0 GPa to investigate the compression and thermal expansion relationships of PIs. The PMDA/ODA and PMDA/SDA PIs showed extraordinary negative compressibility along the *c*-axis, due to the widening of the bond angles at bent linkages (θ_{C-O-C} and θ_{C-S-C}). In addition, PMDA/SDA showed a larger local maximum of ε_c (ε_c^{max}=1.5%) than PMDA/ODA (ε_c^{max}=1.2%). Moreover, both PIs showed large anisotropy between ε_a and ε_b with a larger compression along the *b*-axis that corresponds to the cofacial stacking direction of phenyl and imide rings. These results are explainable by an increase in the angles of θ_{C-O-C} and θ_{C-S-C} that are related to the decrease in the torsional angles around the bent linkages and the larger compression along the *b*-axis than the *a*-axis. On the other hand, the *c* values of the PMDA/TPE and PMDA/BAPB PIs monotonically decreased at elevated pressures, and both PIs showed small anisotropies in compression along the *ab* plane despite the plural ether (–O–) linkages of the diamine moieties. These results are explained by both PIs not having well-aligned cofacial stacking directions. Overall, this study of the compression behavior of PIs with bent, flexible linkages along the main chains at elevated pressures provides valuable information for the correlation between primary chemical structures and crystalline/aggregation structures under extreme conditions, namely at high pressures and temperatures. This knowledge is also beneficial for understanding the molecular aggregation structures of PIs in the solid-state that are closely correlated with a wide range of physical properties of PI materials.

Acknowledgements

This work was supported in part by Grants-in-Aid for Scientific Research, Japan Society for the Promotion of Science (15K13782 and 25288096). The synchrotron radiation experiments were

performed at the BL-10C of High Energy Accelerator Research Organization with the approval of the Photon Factory Program Advisory Committee (Proposal No. 2018G651).

References

1. C. E. Sroog, *J. Polym. Sci. Macromol. Rev.*, **11** (1976) 161.
2. K. Kaneshiro and N. Akahori, "New Revision Latest Polyimide -Basics and Application-, Volume 2 Part II Chapter 2 Polyimide Industrial Materials," Pub. Co., NTS, 2011.
3. J. Ishii, S. Horii, N. Sensui, M. Hasegawa, L. Vladimirov, M. Kochi, and R. Yokota, *High Perform. Polym.*, **21** (2009) 282.
4. S. H. Tuichiev, L. N. Korzahavin, O. Y. Prokhorov, and B. M. Ginzburg, *U.S.S.R. Acad. Sci.*, **7** (1969) 1463.
5. R. Ishige, T. Masuda, Y. Kozaki, E. Fujiwara, T. Okada, and S. Ando, *Macromolecules*, **50** (2017) 2112.
6. Y. Nagata, Y. Ohnishi, and T. Kajiyama, *Polym. J.*, **28** (1996) 980.
7. N. R. Prokopchuk, Y. G. Baklagina, L. N. Korzhavin, A. V. Sidorovich, and M. M. Koton, *Polym. Sci. U.S.S.R.*, **19** (1977) 1297.
8. L. G. Kazaryan, D. Y. Tsvankin, B. M. Ginzburg, S. Tuichiev, L. N. Korzhavin, and S. Y. Frenkel, *Polym. Sci. U.S.S.R.*, **14** (1972) 1344.
9. K. Okuyama, H. Sakaitani, and H. Arikawa, *Macromolecules*, **25** (1992) 7261.
10. T. W. Poon, R. F. Saraf, and B. D. Silverman, *Macromolecules*, **26** (1993) 3369.
11. J. Liu, S. Z. D. Cheng, F. W. Harris, B. S. Hsiao, and K. H. Gardner, *Macromolecules*, **27** (1994) 989.
12. N. Takahashi, D. Y. Yoon, and W. Parrish, *Macromolecules*, **17** (1984) 2583.
13. B. J. Factor, T. P. Russell, and M. F. Toney, *Macromolecules*, **26** (1993) 2847.
14. Y. Obata, K. Okuyama, S. Kurihara, Y. Kitano, and T. Jinda, *Macromolecules*, **28** (1995) 1547.
15. A. Polyimide and O. Poly, *J. Polym. Sci. Part B: Polym. Phys.*, **32** (1994) 2705.
16. K. Wakabayashi, S. I. Kohama, S. Yamazaki, and K. Kimura, *Polymer*, **48** (2007) 458.
17. K. Wakabayashi, S. I. Kohama, S. Yamazaki, K. Kimura, *Macromolecules*, **41** (2008) 1168.
18. J. Wakita, S. Jin, T. J. Shin, M. Ree, and S. Ando, *Macromolecules*, **43** (2010) 1930.
19. K. Takizawa, H. Fukudome, Y. Kozaki, and S. Ando, *Macromolecules*, **47** (2014) 3951.
20. K. Takizawa, J. Wakita, M. Kakiage, H. Masunaga, and S. Ando, *Macromolecules*, **43** (2010) 2115.
21. E. J. Samuelsen, J. Mårdalen, O. R. Konestabo, M. Hanfland, and M. Lorenzen, *Synth. Met.*, **101** (1999) 98.
22. M. Lorenzen, M. Hanfland, and A. Mermet, *Nucl. Instrum. Meth. B*, **200** (2003) 416.
23. E. D. Emmons, R. G. Kraus, S. S. Duvvuri, J. S. Thompson, and A. M. Covington, *J. Polym. Sci. Part B: Polym. Phys.*, **45** (2007) 358.
24. R. G. Kraus, E. D. Emmons, J. S. Thompson, and A. M. Covington, *J. Polym. Sci. Part B: Polym. Phys.*, **46** (2008) 734.
25. B. Yu, Y. Wang, L. Wang, X. Tan, Y.M. Zhang, K. Wang, M. Li, B. Zou, and S. X. A. Zhang, *Phys. Chem. Chem. Phys.*, **21** (2019) 17696.
26. J. W. Hanford, J. G. Koomey, L. E. Stewart, M. E. Lecar, R. E. Brown, F. X. Johnson, R. J. Hwang, and L. K. Price, "Baseline Data for the Residential Sector and Development of a Residential Forecasting Database", Lawrence Berkeley National Laboratory, (1994) LBL-33717.
27. G. Yang, Z. A. Dreger, Y. Li, and H. G. Drickamer, *J. Phys. Chem. A*, **101** (1997) 7948.
28. K. Paudel, H. Knoll, M. Chandrasekhar, and S. Guha, *J. Phys. Chem. A*, **114** (2010) 4680.
29. S. Guha, M. Chandrasekhar, U. Scherf, and M. Knaapila, *Phys. Status Solidi Basic Res.*, **248** (2011) 1083.
30. S. Guha and M. Chandrasekhar, *Phys. Status Solidi Basic Res.*, **241** (2004) 3318.
31. X. Chen, Z. He, F. Kausar, G. Chen, Y. Zhang, and W. Z. Yuan, *Macromolecules*, **51** (2018) 9035.
32. K. Takizawa, J. Wakita, S. Azami, and S. Ando, *Macromolecules*, **44** (2011) 349.
33. E. Fujiwara, H. Fukudome, K. Takizawa, R. Ishige, and S. Ando, *J. Phys. Chem. B*, **122** (2018) 8985.
34. E. Fujiwara, R. Ishige, S. Owaki, N. Kita, K. Yamada, T. Matsuoka, S. Sasaki, and S. Ando, *J. Photopolym. Sci. Technol.*, **31** (2018) 599.
35. G. J. Piermarini, S. Block, and J. D. Barnett, *J. Appl. Phys.*, **44** (1973) 5377.
36. W. Ma, B.-P. Li, and S. Liang, *Z. Krist.-New Crist. St.*, **235** (2020) 219.
37. A. R. Choudhury, K. Islam, M. T. Kirchner, G. Mehta, and T. N. G. Row, *J. Am. Chem. Soc.*, **126** (2004) 12274.
38. B. J. Tabor, E. P. Magré, and J. Boon, *Eur. Polym. J.*, **7** (1971) 1127.